Supporting information

Hybridized piezoelectric-triboelectric effects for self-powered sensing in thermally drawn nancomposite fibers

*Syed Zubair Hussain, Vishwa Pratap Singh, Maliha Rahman, Deniz Berk Onuralp, and Mustafa Ordu**

UNAM National Nanotechnology Research Center and Institute of Materials Science and Nanotechnology, Bilkent University, Ankara 06800, Türkiye

* E-mail: ordu@unam.bilkent.edu.tr

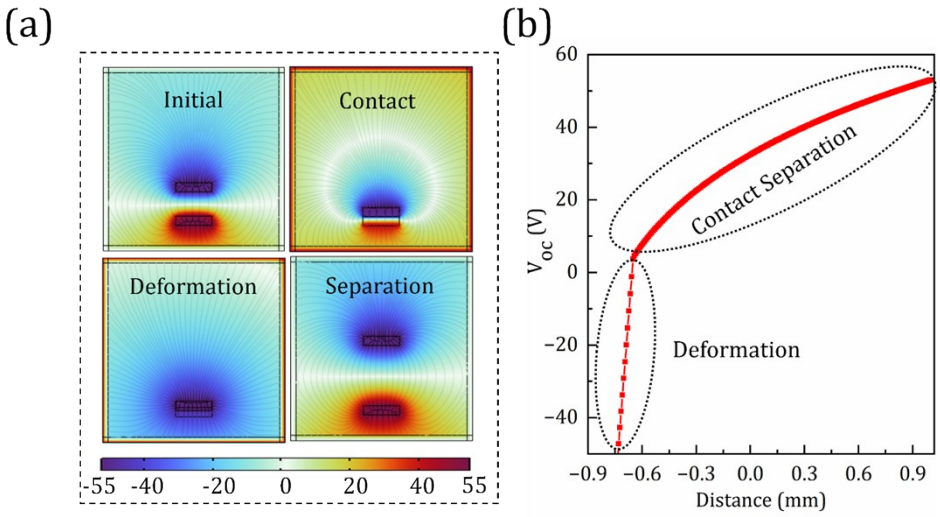

Figure S1. Numerical modelling of PT-HNG fiber. (a) Demonstration of contact-separation of the fiber. (b) The plot shows the trend of voltage generation with the contact separation and deformation-release.

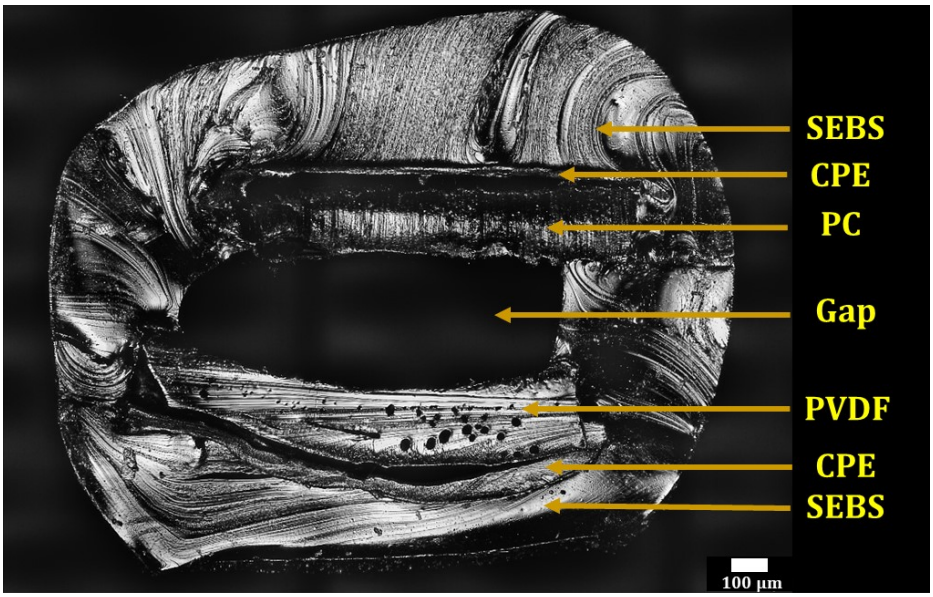

Figure S2. Laser DIC image of the fiber cross-section. Scale bar: 100 µm.

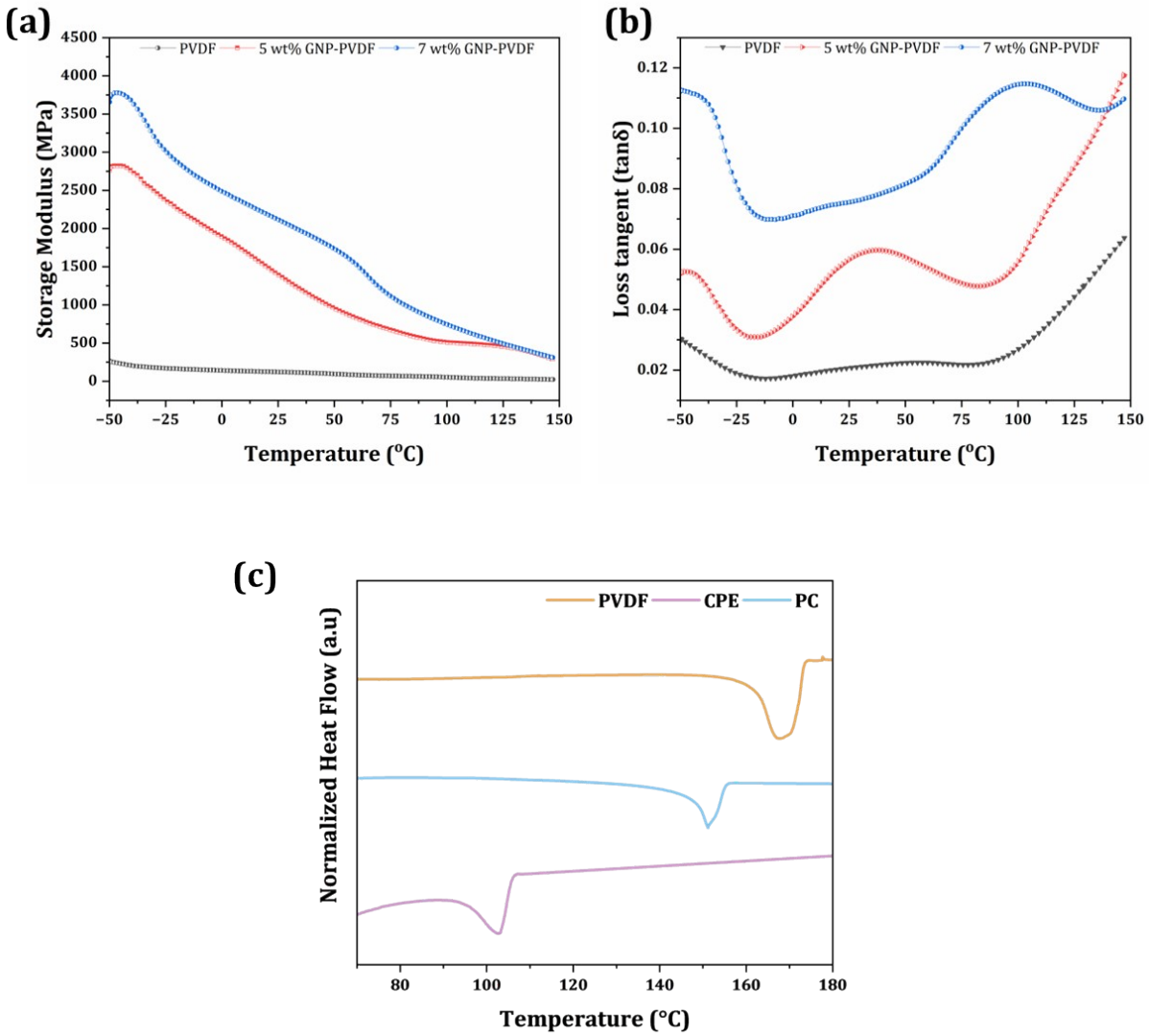

Figure S3. (a) Storage modulus and (b) loss tangent as a function of temperature. (c) DSC curve of the polymers used as the preform for fiber fabrication; CPE melting temperature is 102.7 °C, PVDF melting temperature is 168 °C, and PC glass transition temperature is 151.2 °C.

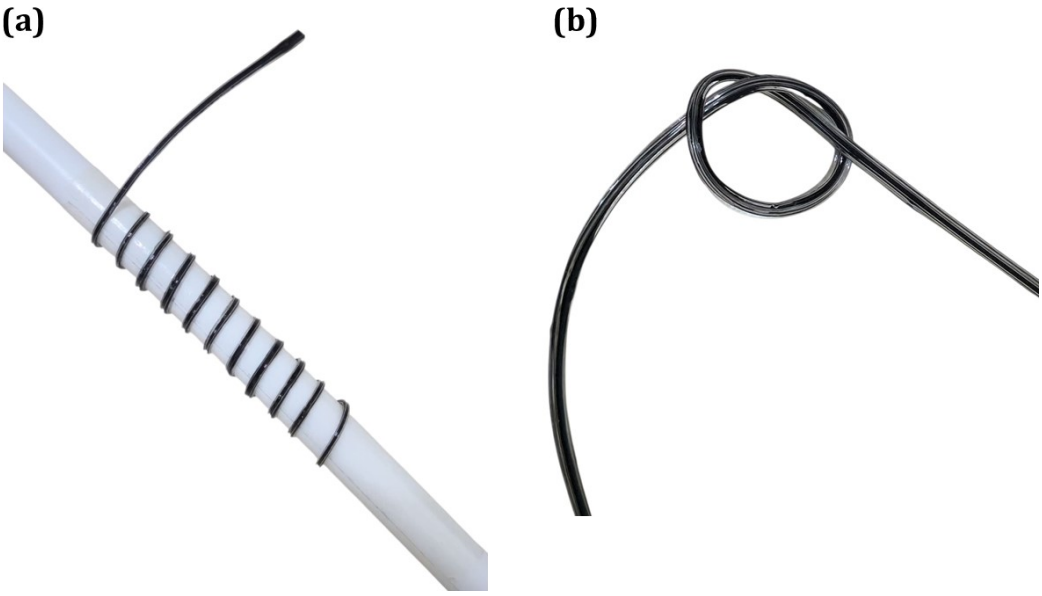

Figure S4. Flexibility of the fiber, (a) bending and (b) knotting.

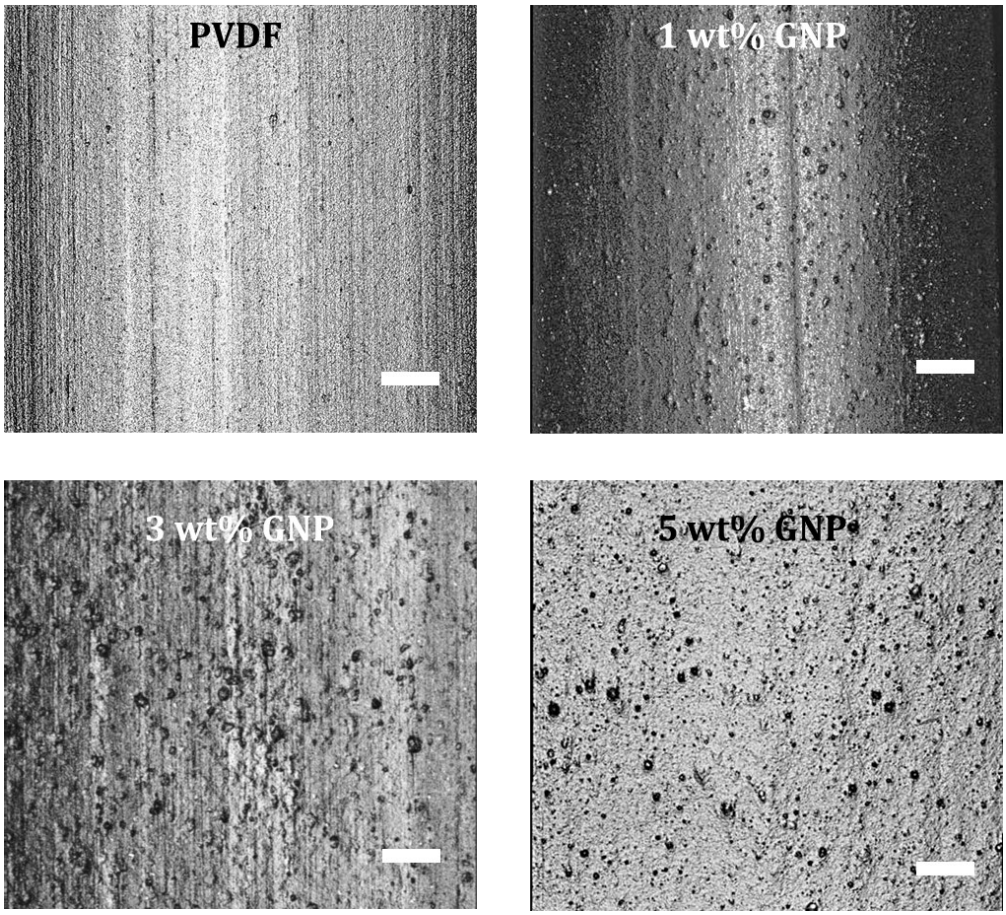

Figure S5. Laser DIC image of the pristine PVDF and GNP-PVDF nanocomposite fibers. Scale bar: 100 μm.

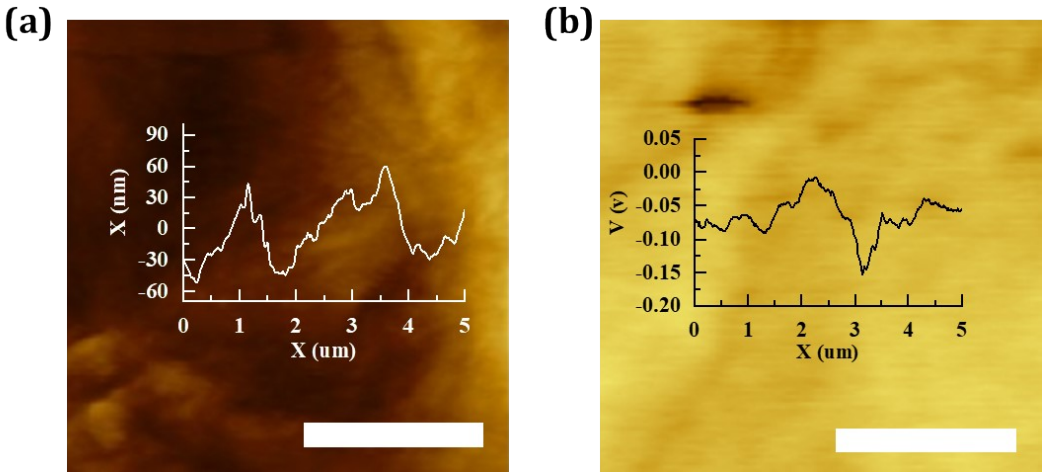

Figure S6. Kelvin probe force microscopy (KPFM) analysis of pristine PVDF. (a) Surface topography (height/roughness) profile of the PVDF surface, showing nanoscale morphological variations across the scanned region. (b) Line profile of the contact potential difference (V_{CPD}) extracted from the KPFM measurement, representing the spatial variation in surface potential. Scale bar: 1 µm.

Figure S7. PT-HNG fiber integrated on a textile waistband.

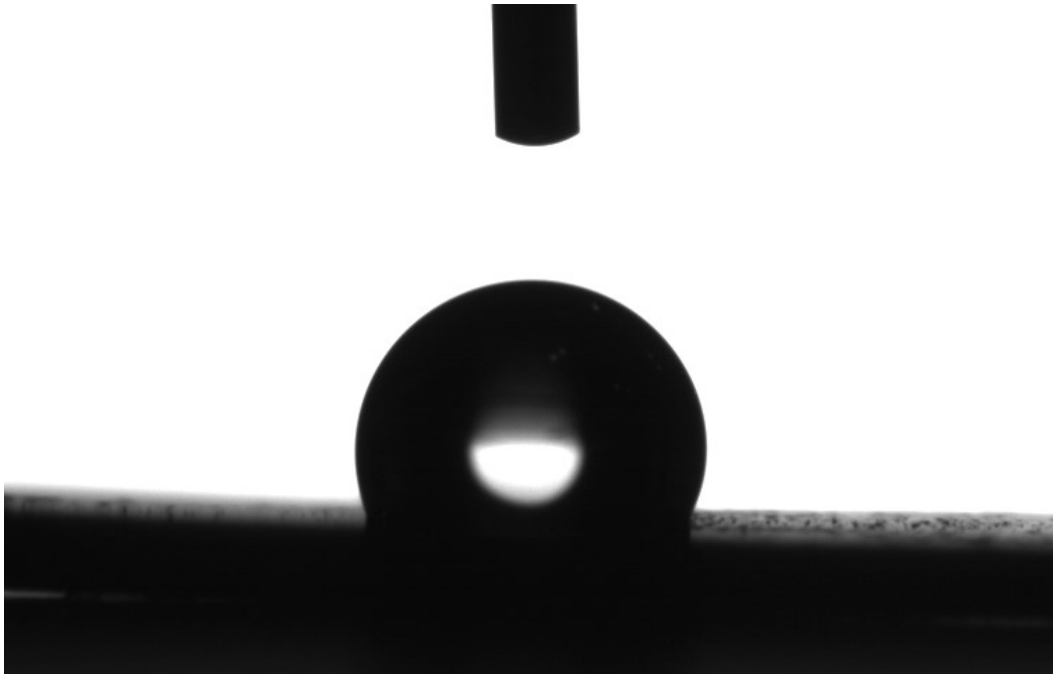

Figure S8. Contact angle measurement shows the hydrophobic nature of 5 wt% GNP-PVDF nanocomposite fibers (112.4°).

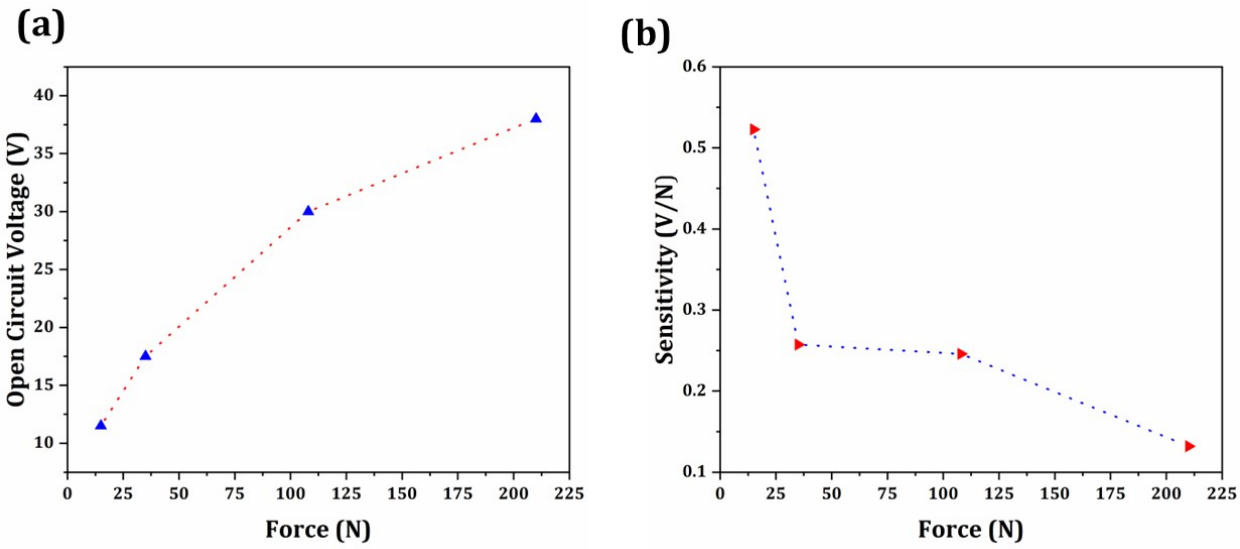

Figure S9. Open-circuit voltage as a function of applied force. (b) Force-dependent sensitivity of the fiber, calculated as S=V/F.

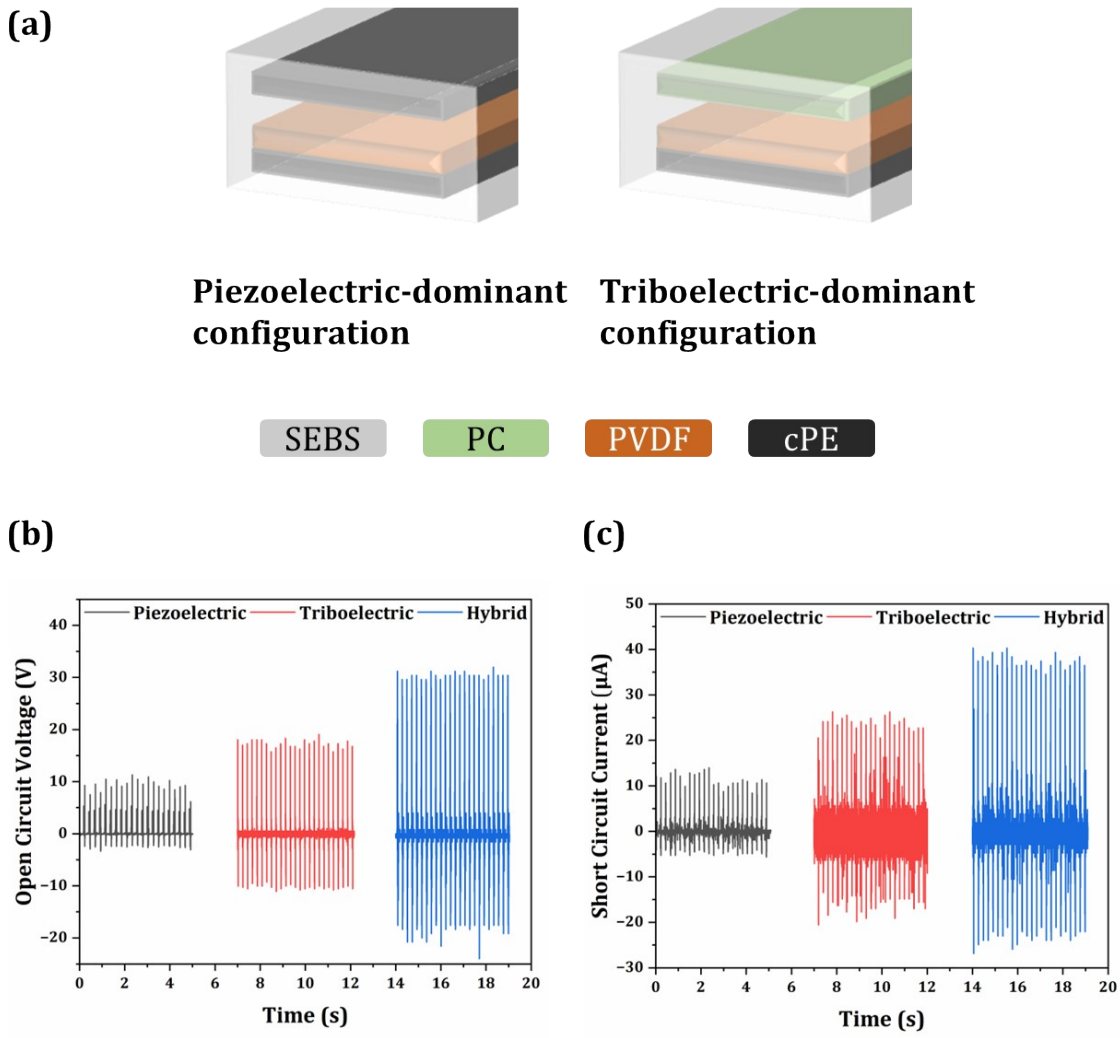

Figure S10. Experimental comparison of piezoelectric-dominant, triboelectric-dominant, and hybrid outputs of the PT-HNG fiber under identical tapping conditions. (a) Schematic illustration of the modified device configurations used to isolate the dominant contribution of each mechanism. (b) Open-circuit voltage and (c) short-circuit current measured from the piezoelectric-dominant, triboelectric-dominant, and intact hybrid configurations.

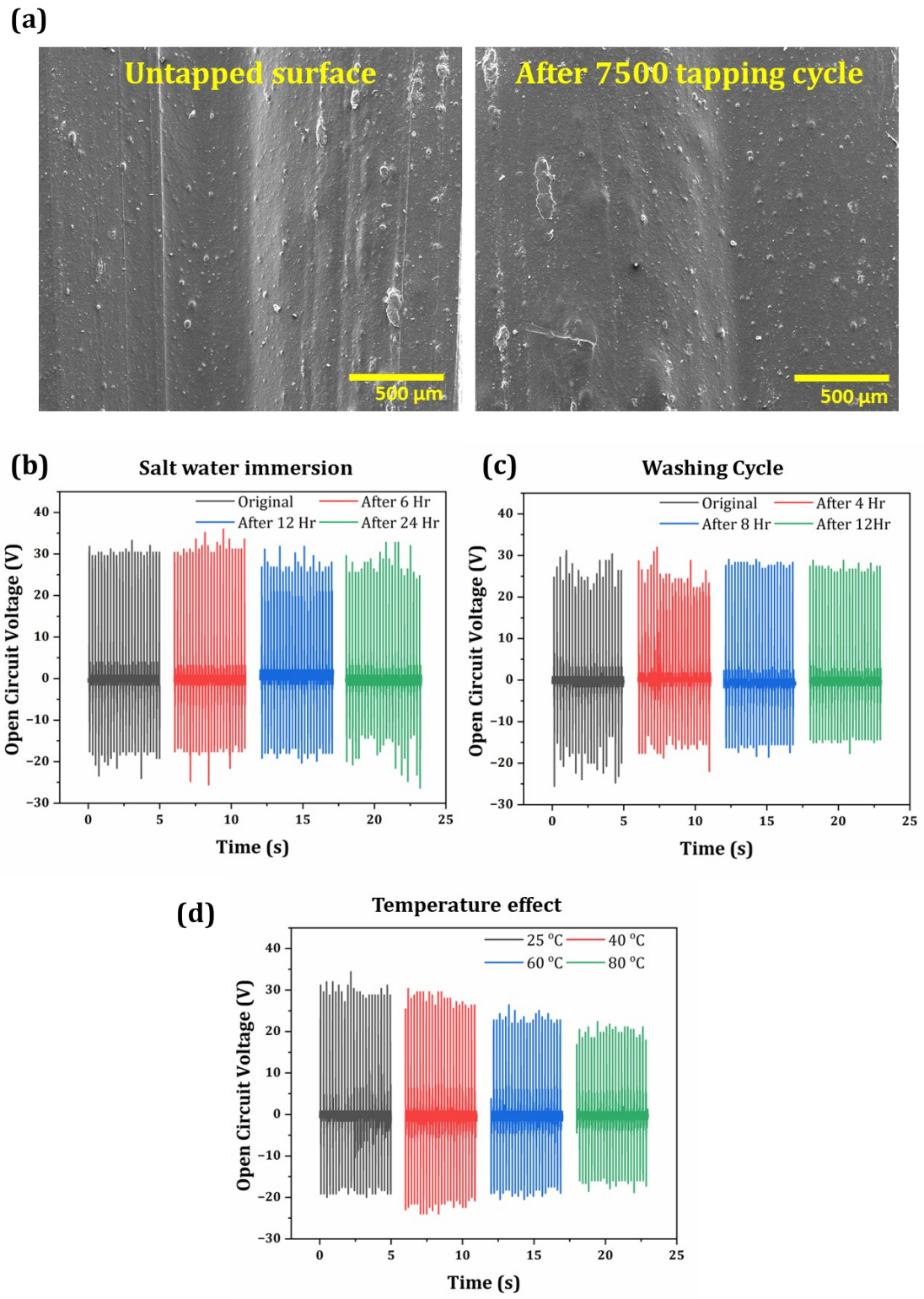

Figure S11. Environmental stability and durability of the PT-HNG fiber. (a) Surface morphology of the PVDF-based functional layer before and after 7500 tapping cycles. (b) Electrical output before and after washing and salt water immersion (4 wt% NaCl solution). (c) Output performance of the fiber after exposure to elevated temperatures.

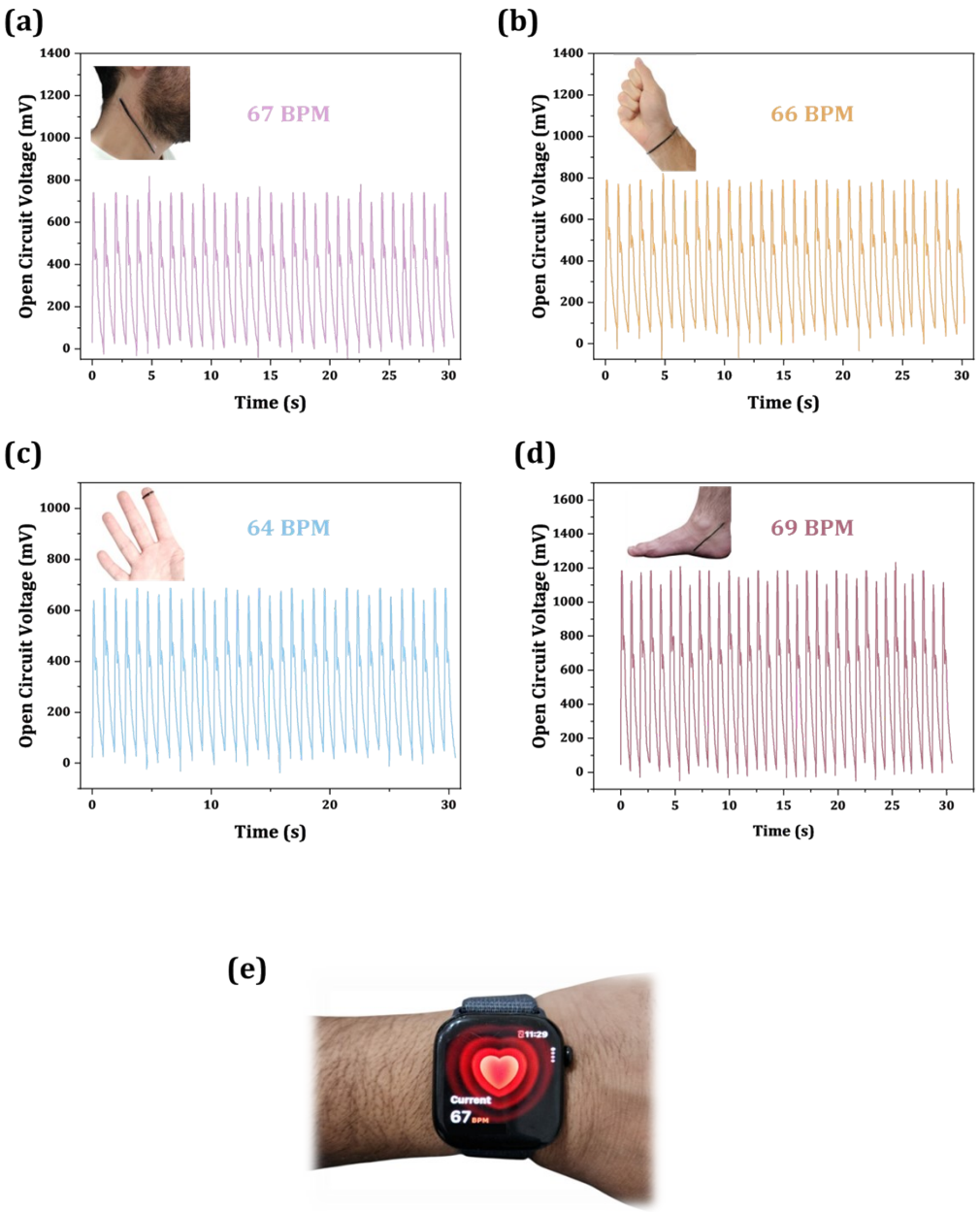

Figure S12. Pulse waveform at different locations for 30 s. Fiber sensor output when attached to (a) neck, (b) wrist, (c) fingertip, and (d) ankle.

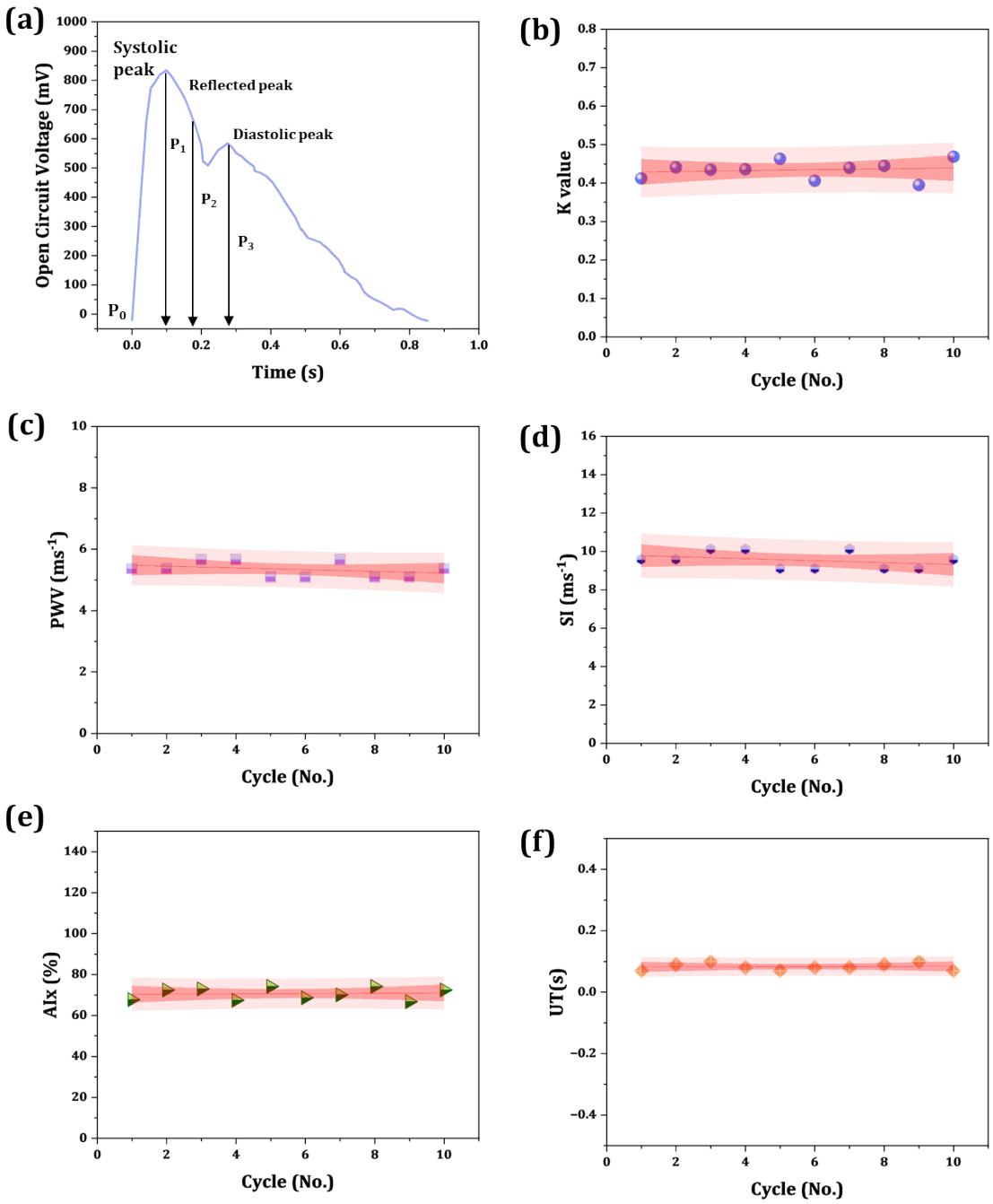

Figure S13. (a) Single pulse cycle waveform from the wrist. Cardiovascular parameters analysis, (b) K value, (c) pulse wave velocity (PWV), (d) stiffness index (SI), (e) radial augmentation index (AIx), and (f) upstroke time (UT) for 10 consecutive pulse cycles. The dark and light-shaded regions indicate 95% confidence and 95% prediction bands, respectively.

Table S1. Cardiovascular parameters of representative individuals.

Parameters	Mean	Standard deviation	Median
K value	0.43391	0.02364	0.43744
PWV	5.35068	0.24764	5.36842
SI	9.54702	0.44183	9.57895
AIx	70.68236	2.88036	71.23694
UT	0.08400	0.01174	0.08500

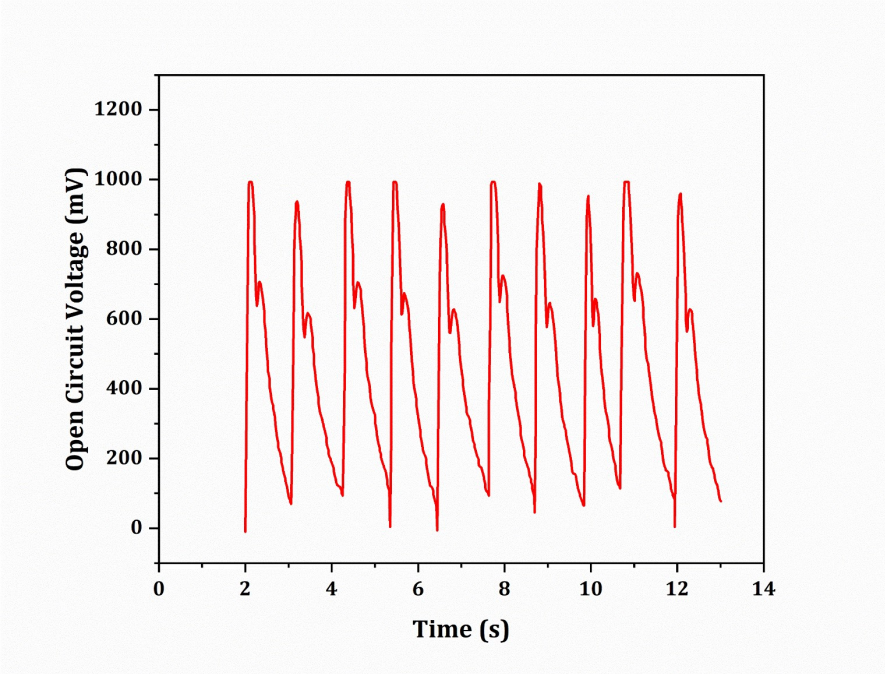

Figure S14. Representative waveform used to calculate cardiovascular parameters.

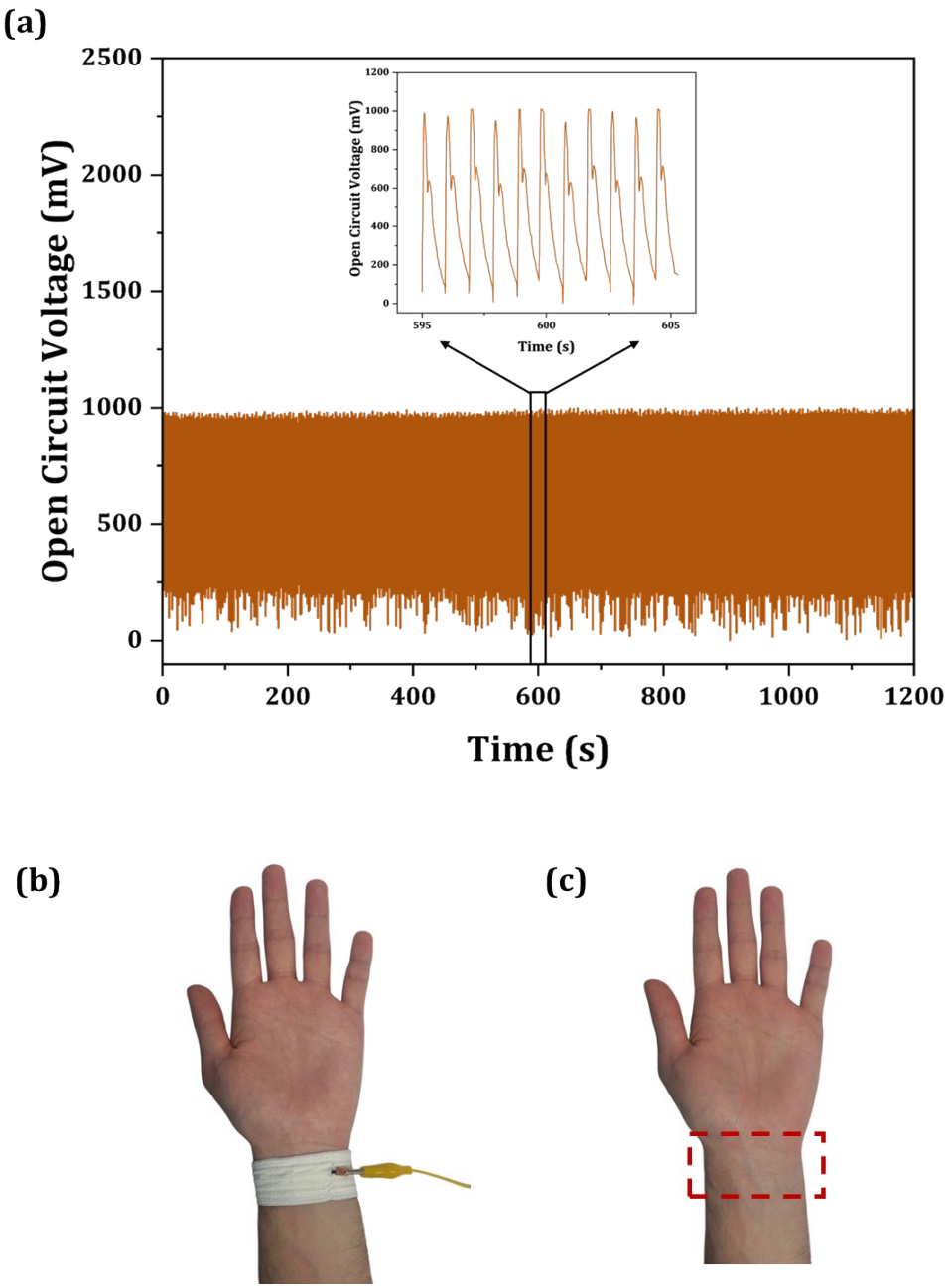

Figure S15. Wearable demonstration of the PT-HNG fiber for physiological sensing. (a) A continuous signal recorded from the wrist around 20 minutes. (b) Photograph of the PT-HNG fiber integrated onto the wrist for pulse monitoring. (c) Optical image of the skin after prolonged wearing (~30 minutes).

Table S2. Development fiber based thermally drawn nanogenerators.

System	Device Type	Power (μW)	Power Density (mW/m²)	Ref.
MoS_2-PVDF PENG	Single fiber	5.78	0.5	[1]
MoS_2-PVDF TENG	Single fiber	17.64	—	[2]
MXenePVDF TENG	Fabric (3 cm × 2 cm)	24.5	40.8	[3]
GNP-PVDF TENG	Fabric (3 cm × 2 cm)	32.14	53.57	[4]
GNP-PVDF PT-HNG	Single fiber	21	266.27	**This work**

Supporting Note 1. Finite element analysis of the PT-HNG fiber.

Finite element simulations were performed using COMSOL Multiphysics to better understand the electromechanical behavior of the piezo-triboelectric hybrid nanogenerator (PT-HNG) fiber. The simulated geometry closely resembled the experimentally fabricated thermally drawn fiber, consisting of SEBS as the outer cladding, conductive polyethylene (cPE) electrodes, a tribo-positive polycarbonate (PC) layer, and a tribo-negative GNP-PVDF nanocomposite layer separated by an air gap. The GNP-PVDF layer was modeled with a dielectric constant of 47 and a piezoelectric coefficient of -23 [5]. The triboelectric surface charge density was determined from KPFM measurements, where the PVDF exhibited a work function of 5.27 eV at a 100 nm tip-sample distance using a PtIr probe. A sinusoidal compressive load of 50 N was applied using the Solid Mechanics module, while the coupled electrostatic behavior was analyzed through a finely meshed model to ensure numerical precision.

The simulation revealed the potential distribution and voltage response across four operational stages: initial, contact, deformation, and separation. During the separation phase, triboelectric charge transfer between the PC and PVDF layers generated a floating potential of approximately 55 V, while the deformation of the PVDF layer produced a piezoelectric voltage of about -42 V due to its negative piezoelectric coefficient (**Video S1**). The overall voltage response demonstrated that the hybrid fiber benefits from the synergistic coupling of triboelectric and piezoelectric mechanisms, where triboelectric charge accumulation enhances the interfacial potential difference and the piezoelectric polarization further amplifies the output during deformation. This combined effect results in superior charge utilization and improved energy-conversion efficiency, confirming that the hybrid design maximizes electrical output compared to individual mechanisms.

Supporting Note 2. PT-HNG fiber for cardiovascular sensing [6].

To demonstrate the capability of the PT-HNG fiber in cardiovascular monitoring, characteristic pulse waveforms were recorded from the wrist and analyzed to extract multiple hemodynamic indicators. Each cardiac cycle contains distinctive points corresponding to the diastolic foot (P_0), systolic peak (P_1), reflected peak (P_2), and dicrotic peaks. These parameters were used to calculate clinically relevant indices describing vascular stiffness, elasticity, and cardiac function.

K value represents the relationship between mean arterial pressure and the systolic–diastolic range, reflecting vascular elasticity and peripheral resistance.

$$K = \frac{(P_m - P_0)}{(P_1 - P_0)} \tag{S1}$$

where P_0 is the diastolic pressure, P_1 is the systolic peak, and P_m is the mean pressure within one cycle. The mean pressure is obtained by integrating the pulse over one period t:

$$P_m = \left(\frac{1}{t}\right)\int_0^t P(\tau)d\tau \tag{S2}$$

Typical values below 0.35 correspond to low vascular resistance, indicative of good arterial elasticity in healthy adults.

Pulse Wave Velocity (PWV) measures the propagation speed of the pressure wave and serves as a primary marker of arterial stiffness.

$$PWV = 0.8 \times \frac{(2 \times \Delta L)}{RWTT} \tag{S3}$$

where ΔL is the distance between the suprasternal notch and the umbilicus (approximating the jugulum-pubic path), and RWTT is the time between the systolic and reflected peaks. The factor 0.8 accounts for empirical path correction. Higher PWV values indicate increased arterial stiffness.

Stiffness index (SI) correlates with the large-artery pulse velocity and is calculated from the subject's height and the time between diastolic and systolic peaks.

$$SI = \frac{H}{PPT} \tag{S4}$$

where H is the body height and PPT = t_1 -t_0 is the time between the diastolic foot and the systolic peak. Comparable SI and PWV values confirm consistent stiffness estimation.

Radial Augmentation Index (AIx) quantifies the contribution of the reflected wave to the overall systolic amplitude and is closely linked to vascular aging.

$$AIx = \left(\frac{P_2}{P_1}\right) \times 100\% \tag{S5}$$

where P_1 and P_2 are the systolic and reflected peaks, respectively. For healthy young subjects, AIx typically ranges between 50-65%.

Upstroke Time (UT) represents the time taken for the pulse to rise from the diastolic baseline to the systolic maximum, reflecting the rate of blood ejection from the left ventricle.

$$UT = t_1 - t_0 \quad \text{(S6)}$$

Shorter UT corresponds to faster ventricular ejection and higher arterial compliance.

Supporting Note 3. Signal-to-noise ratio (SNR) analysis.

To quantitatively evaluate the signal quality of the fiber sensor, the SNR was calculated by comparing the amplitude of the physiological signal to the baseline noise level. The baseline noise was recorded under static conditions, where the fiber sensor was not subjected to any external mechanical stimulation. The active signal was recorded during physiological events, such as respiration or pulse, during which periodic deformation of the fiber generated a measurable electrical response.

The SNR was calculated from the root-mean-square (RMS) values of the signal and noise. The RMS value of the active signal (x_{signal}) represents the useful physiological response, while the RMS value of the baseline (x_{noise}) represents the background noise level. The SNR in decibels (dB) was determined using the following equation:

$$SNR(dB) = 20log\frac{RMS_{(x_{signal})}}{RMS_{(x_{noise})}} \tag{S7}$$

where,

$$RMS(x) = \sqrt{\frac{1}{N}\sum_{i=1}^{N} x_i^2} \tag{S8}$$

and N is the total number of sampled data points.

Using this method, the fiber sensor demonstrated SNR of 25.2 dB, indicating that the physiological signal is significantly distinguishable from background noise and demonstrating the device's capability for reliable self-powered sensing.

Videos

1. Video S1. Finite element analysis
2. Video S2. LEDs powered by PT HNG fiber
3. Video S3. Wrist pulse monitoring
4. Video S4. Neck pulse monitoring

References

[1] M. M. Hasan, M. Rahman, M. S. B. Sadeque, and M. Ordu, "Self-Poled Piezoelectric Nanocomposite Fiber Sensors for Wireless Monitoring of Physiological Signals," *ACS Appl. Mater. Interfaces*, vol. 16, no. 27, pp. 34549–34560, Jul. 2024, doi: 10.1021/acsami.4c04908.

[2] M. S. B. Sadeque, M. Rahman, M. M. Hasan, and M. Ordu, "Thermal Drawing of MoS2 Integrated PVDF Triboelectric Fiber for Continuous Respiration Monitoring," *Adv. Sens. Res.*, vol. 4, no. 3, p. 2400114, 2025, doi: 10.1002/adsr.202400114.

[3] M. M. Hasan *et al.*, "Scalable Fabrication of MXene-PVDF Nanocomposite Triboelectric Fibers via Thermal Drawing," *Small*, vol. 19, no. 6, p. 2206107, 2023, doi: 10.1002/smll.202206107.

[4] M. S. B. Sadeque, M. Rahman, M. M. Hasan, and M. Ordu, "Graphene Nanoplatelet Integrated Thermally Drawn PVDF Triboelectric Nanocomposite Fibers for Extreme Environmental Conditions," *Adv. Electron. Mater.*, vol. 10, no. 4, p. 2300643, 2024, doi: 10.1002/aelm.202300643.

[5] V. P. Singh, A. K. Singh, and M. Ordu, "Nanointerface Insights in PVDF Films with Low Loading of Nitrogen-Doped Carbon Dots for High Energy Density Storage and Harvesting," *ACS Appl. Electron. Mater.*, vol. 7, no. 3, pp. 1080–1094, Feb. 2025, doi: 10.1021/acsaelm.4c01882.

[6] Y. Zhou *et al.*, "Giant magnetoelastic effect in soft systems for bioelectronics," *Nat. Mater.*, vol. 20, no. 12, pp. 1670–1676, Dec. 2021, doi: 10.1038/s41563-021-01093-1.